(Preprint) AAS 23-189

BACKBONE OF BALLISTIC CAPTURE SET

Gianmario Merisio*, and Francesco Topputo†

Currently, deep-space missions strongly rely on ground-based operations. Although reliable, ground slots will saturate soon, hampering current momentum in space exploration. EXTREMA, a project awarded an ERC Consolidator Grant in 2019, enables self-driving spacecraft, challenging the current paradigm and aiming at autonomously engineering ballistic capture. Deep-space GNC applied in a complex scenario is its subject. The paper defines the backbone of a ballistic capture set and presents a methodology based on Lagrangian descriptors for its derivation. Orbits belonging to capture sets up to $\mathcal{C}_{-1}^{10}$ are inferred from the backbone. The method constitutes a block of the autonomous ballistic capture algorithm.

INTRODUCTION

The space sector is experiencing flourishing growth and evidence is mounting that the near future will be characterized by a large amount of deep-space missions.[1–3] In the last decade, CubeSats have granted affordable access to space due to their reduced manufacturing costs compared to traditional missions. At the present-day, most miniaturized spacecraft have thus far been deployed into near-Earth orbits, but soon a multitude of interplanetary CubeSats will be employed for deep-space missions as well. However, the current paradigm for deep-space missions strongly relies on ground-based operations. Although reliable, this approach will rapidly cause saturation of ground slots, hampering the current momentum in space exploration.

EXTREMA (Engineering Extremely Rare Events in Astrodynamics for Deep-Space Missions in Autonomy) enables self-driving spacecraft, challenging the current paradigm under which spacecraft are piloted in the interplanetary space.[4,5] Deep-space guidance, navigation, and control (GNC) applied in a complex scenario is the subject of EXTREMA. Among others, the project aims to engineer ballistic capture in a totally autonomous fashion. EXTREMA is erected on three pillars. Pillar 1 is about autonomous navigation.[6–8] Pillar 2 concerns autonomous guidance and control.[9,10] Pillar 3 deals with autonomous ballistic capture,[11–13] the focus of this work. The project has been awarded a European Research Council (ERC) Consolidator Grant in 2019.

Ballistic capture allows a spacecraft to approach a planet and enter a temporary orbit about it without requiring maneuvers in between.[14–16] The mechanism is suited for limited-control platforms, which cannot afford to enter into orbits about a planet because of the lack of proper means.[11–13] In Pillar 3, the spacecraft assumed already in deep space has to acquire ballistic capture at Mars autonomously and without relying on any information provided from the ground. The challenge is to develop and validate an algorithm compatible with the onboard resources. In this work, the backbone of a capture set is introduced and the methodology for its derivation is presented. The methodology constitutes a required building block of the autonomous ballistic capture algorithm.[13]

*PhD Candidate, Dept. of Aerosp. Sci. and Technol., Politecnico di Milano, Via La Masa 34, 20156, Milano, Italy.
†Full Professor, Dept. of Aerosp. Sci. and Technol., Politecnico di Milano, Via La Masa 34, 20156, Milano, Italy.

Table 1. Spacecraft parameters for SRP evaluation.[21]

Parameter	Unit	Value
Mass–SRP area ratio m/A	$\mathrm{kg\,m^{-2}}$	75
Coefficient of reflectivity C_r	-	1.3

BACKGROUND

Dynamics

Following the nomenclature in Reference 15, a *target* and a *primary* are defined. The target is the body around which the ballistic capture is studied. The primary is the main body around which the target revolves. Target and primary masses are m_t and m_p, respectively. The mass ratio of the system is $\mu = m_t/(m_t + m_p)$. In this work, Mars is the target and the Sun is primary.

Reference frames. The following reference frames are used: J2000, and RPF.

J2000. Defined on Earth's mean equator and equinox, J2000 is an inertial frame determined from observations of planetary motions, which was realized to coincide almost exactly with the International Celestial Reference Frame (ICRF).[17] The J2000 inertial frame (also known as EMEJ2000) is built-in in SPICE.[18,19] In SPICE, the ICRF and J2000 frames are considered the same. The origin of the J2000 can be chosen arbitrarily.

RTN@t_i. The radial-tangential-normal of date frame (RTN@t_i) is an inertial frame frozen at a prescribed epoch t_i. The frame is centered at the target. The x-axis is aligned with the primary–secondary direction, the z-axis is normal to the primary–secondary plane in the direction of their angular momentum, and the y-axis completes the dextral orthonormal triad.

Ephemerides. The precise states of the Sun and the major planets are retrieved from the Jet Propulsion Laboratory (JPL)'s planetary ephemerides `de440s.bsp`* (or DE440s).[20] Additionally, the ephemerides `mar097.bsp` of Mars (the target) and its moons are employed†. Unless otherwise specified, the following generic leap seconds kernel (LSK) and planetary constant kernel (PCK) were used: `naif0012.tls`, `pck00010.tpc`, and `gm_de440.tpc`‡.

Equations of motion. The Equations of motion (EoM) of the restricted n-body problem are considered. Unless otherwise specified, the gravitational attractions of the Sun, Mercury, Venus, Earth (B§), Mars (central body), Jupiter (B), Saturn (B), Uranus (B), and Neptune (B) are taken into account. Additionally, solar radiation pressure (SRP) is also included in the model. The assumed spacecraft parameters needed to evaluate the SRP perturbation are collected in Table 1. They are compatible with the parameters of a 12U deep-space CubeSat.[21] EoM are integrated in the J2000 inertial frame.

*Data publicly available at: `https://naif.jpl.nasa.gov/pub/naif/generic_kernels/spk/planets/de440s.bsp` [retrieved Jan 5, 2023].

†`~/spk/satellites/mar097.bsp` [retrieved Jan 5, 2023].

‡Data publicly available at: `https://naif.jpl.nasa.gov/pub/naif/generic_kernels/lsk/naif0012.tls`, and `~/generic_kernels/pck/pck00010.tpc` [retrieved Jan 5, 2023]. The `gm_de440.tpc` PCK kernel was written from scratch, courtesy of Dr. C. Giordano, because the version consistent with ephemerides DE440s is not released yet.

§Here B stands for barycenter.

Table 2. First set of nondimensionalization units.

Unit	Symbol	Value	Comment
Gravity parameter	$\bar{\mathrm{MU}}$	$42\,828.376\,\mathrm{km^3\,s^{-2}}$	Mars' gravity parameter μ_t
Length	$\bar{\mathrm{LU}}$	$1.085\,772\times10^{6}\,\mathrm{km}$	Mars–$L_{2,\odot\mathord{\male}}$ distance
Time	$\bar{\mathrm{TU}}$	$5.466\,913\times10^{6}\,\mathrm{s}$	$(\bar{\mathrm{LU}}^3/\bar{\mathrm{MU}})^{0.5}$
Velocity	$\bar{\mathrm{VU}}$	$1.986\,079\times10^{-1}\,\mathrm{km\,s^{-1}}$	$\bar{\mathrm{LU}}/\bar{\mathrm{TU}}$

Table 3. Second set of nondimensionalization units.

Unit	Symbol	Value	Comment
Gravity parameter	MU	$42\,828.376\,\mathrm{km^3\,s^{-2}}$	Mars' gravity parameter μ_t
Length	LU	$3396.0000\,\mathrm{km}$	Mars' radius $R_{\male}$
Time	TU	$956.281\,42\,\mathrm{s}$	$(\mathrm{LU}^3/\mathrm{MU})^{0.5}$
Velocity	VU	$3.551\,255\,8\,\mathrm{km\,s^{-1}}$	LU/TU

The EoM in a non-rotating Mars-centered reference frame are[15,22,23]

$$\ddot{\mathbf{r}} = -\frac{\mu_t}{r^3}\mathbf{r} - \sum_{i\in\mathbb{P}}\mu_i\left(\frac{\mathbf{r}_i}{r_i^3} + \frac{\mathbf{r}-\mathbf{r}_i}{\|\mathbf{r}-\mathbf{r}_i\|^3}\right) + \frac{QA}{m}\frac{\mathbf{r}-\mathbf{r}_\odot}{\|\mathbf{r}-\mathbf{r}_\odot\|^3} \tag{1}$$

where μ_t is the gravitational parameter of the target body (i. e., Mars in this work); $\mathbf{r}$ and $\dot{\mathbf{r}} = \mathbf{v}$ are the position and velocity vectors of the spacecraft with respect to the target, respectively, being r and v their magnitudes; $\mathbb{P}$ is a set of $n-2$ indexes (where n concerns the n-body problem) each one referring to the perturbing bodies; μ_i and $\mathbf{r}_i$ are the gravitational parameter and position vector of the i-th body with respect to the target, respectively; A is the Sun-projected area on the spacecraft for SRP evaluation; m is the spacecraft mass; $\mathbf{r}_\odot$ is the position vector of the Sun with respect to the target. Then, $Q = LC_r/(4\pi c)$ where C_r is the spacecraft coefficient of reflectivity, $c = 299\,792\,458\,\mathrm{m\,s^{-1}}$ (from SPICE[18,19]) is the speed of light in vacuum, and $L = S_\odot 4\pi d_{\mathrm{AU}}^2$ is the luminosity of the Sun. The latter is computed from the solar constant* $S_\odot = 1367.5\,\mathrm{W\,m^{-2}}$ evaluated at distance $d_{\mathrm{AU}} = 1\,\mathrm{AU}$.

Numerical propagation. The EoM in Eq. (1) are integrated with the GRATIS[24] in their nondimensional form to avoid ill-conditioning.[15] Normalization units are reported in Table 2. A second set of normalization units is used in plots for visualization purposes (see Table 3). Numerical integration is carried out with the Dormand–Prince 8th-order embedded Runge–Kutta (DOPRI8) propagation scheme,[25] also known as RK8(7)13M. This is an adaptive step, 8th-order Runge–Kutta (RK) integrator with 7th-order error control. Coefficients were derived by Prince and Dormand.[26] The dynamics are propagated with relative and absolute tolerances both set to 10^{-12} (see Reference 15).

Ballistic capture

Ballistic capture allows a spacecraft to approach a planet and enter a temporary orbit about it without requiring maneuvers in between. As part of the low-energy transfers, it is a valuable alternative to Keplerian approaches. Exploiting ballistic capture (BC) grants several benefits in terms of

*`https://extapps.ksc.nasa.gov/Reliability/Documents/Preferred_Practices/2301.pdf` [last accessed Jan 5, 2023].

both cost reduction[27] and mission versatility,[14,28] in general at the cost of longer transfer times.[29,30] In the past, the BC mechanism was used to rescue Hiten,[31] and to design insertion trajectories in lunar missions like SMART-1[32] and GRAIL.[33] In the near future, BepiColombo will exploit BC orbits to be weakly captured by Mercury.[34,35] BC is an extremely rare event[16] and requires acquiring a proper state far away from the target planet.[14]

BC orbits are characterized by initial conditions (ICs) escaping the target when integrated backward and performing n revolutions about it when propagated forward, neither impacting or escaping the target. In forward time, particles flying on BC orbits approach the target coming from outside its sphere of influence (SOI) and remain temporarily captured about it. After a certain time, the particle escapes if an energy dissipation mechanism does not take place. To make the capture permanent, either a breaking maneuver or the target atmosphere (if available) could be used.[36,37]

When searching for BC opportunities, most of the trajectories found are spurious solutions typically not useful for mission design purposes.[15] Practical solutions are detected via the regularity index* S and regularity coefficient $\Delta S_{\%}$.[39] The aim is seeking for ideal orbits that present regular post-capture legs resulting in n revolutions about the target similar in both orientation and shape. Numerical experiments showed that high-quality, post-capture orbits are associated to small regularity index and coefficient.[15,16,38,39] Capture occurrence is quantitatively measured through the capture ratio $\mathcal{R}_C$.[16] Typically, search spaces characterized by a large capture ratio are desirable when looking for BC orbits.

Weak stability boundary. Over the years, the weak stability boundary (WSB) was defined in several different ways. It was initially identified as a fuzzy boundary region placed at approximately 1.5×10^6 km from the Earth in the Sun–Earth direction.[31,40] An algorithmic definition followed in,[41] later extended in References 42–44. Then, it was interpreted as the intersection of three subsets of the phase space.[45,46] The WSB being closely connected to BC,[41] a formal definition and a methodology for its derivation from weakly stable and unstable sets were finally proposed in Reference 47. The fascinating idea of extending the WSB concept to the interstellar space including dark matter was discussed in Reference.[48] To date, despite the effort put in numerous works (see References 42, 45, 46, 49, 50), both WSB and BC are still not completely understood. Nonetheless, a connection between celestial and quantum mechanics was recently found exploiting the WSB,[51] providing a fresh perspective to tackle the problem.

Definition of particle stability. A particle stability is inferred using a plane in the 3-dimensional physical space.[27] According to the spatial stability definition provided in Reference 15. The following indications are used to classify stability (see Reference 15 for more details): 1) a particle completes a revolution around the target according to *Remark 1* and Eq. (5) in Reference 15; 2) a particle escapes from the target according to *Remark 2* and Eq. (6) in Reference 15; 3) a particle impacts with the target according to *Remark 3* and Eq. (7) in Reference 15. Variants of Eq. (7) in Reference 15 can be derived to locate impacts with target's moons.

Based on its dynamical behavior, a propagated trajectory is said to be: i) *weakly stable* (sub-set $\mathcal{W}_i$) if the particle performs i complete revolutions around the target without escaping or impacting with it or its moons; ii) *unstable* (sub-set $\mathcal{X}_i$) if the particle escapes from the target before completing the ith revolution; iii) *target–crash* (sub-set $\mathcal{K}_i$) if the particle impacts with the target before

*In previous works, this was referred to as stability index.[15,16,38] However, the adjustment from *stability* to *regularity* index was proposed in Reference 39 to avoid misunderstandings with the periodic orbit stability index. The same nomenclature introduced in Reference 39 is used in this paper.

completing the ith revolution; iv) *moon–crash* (sub-set $\mathcal{M}_i$) if the particle impacts with one of the target's moons before completing the ith revolution; v) *acrobatic* (sub-set $\mathcal{D}_i$) if none of the previous conditions occurs within the integration time span. Conditions ii)-v) apply after the particle performs $(i-1)$ revolutions around the target. The sub-sets are defined for $i \in \mathbb{Z}\backslash\{0\}$, where the sign of i informs on the propagation direction. When $i > 0$ ($i < 0$) the IC is propagated forward (backward) in time. The overall domain, union of all sub-sets, is defined Ω. A capture set is defined as $\mathcal{C}^n_{-1} := \mathcal{W}_n \cap \mathcal{X}_{-1}$. Therefore, it is the intersection between the stable set in forward time $\mathcal{W}_n$ and the unstable set in backward time $\mathcal{X}_{-1}$.[15]

Design of ballistic capture orbits. Currently, two approaches are known for designing BC orbits: the technique stemmed from invariant manifolds,[49,52] and the method based on stable sets manipulation.[15,47] The former gives insights into the dynamics but it is only applicable to autonomous systems akin to the circular restricted three-body problem (CR3BP), while the latter can be applied to more representative, non-autonomous models, although being computationally expensive.[16,43] Lately, the variational theory for Lagrangian coherent structures (LCSs),[53,54] and the Taylor differential algebra[55] were applied to derive BC orbits and the WSB more efficiently.[56,57]

Lagrangian descriptors

Lagrangian descriptors (LDs) are a heuristic technique for revealing the underlying template of geometrical structures that determine transport in phase space for a generic dynamical system.[58] They are based on the integration of a bounded, positive property of the trajectory over a finite horizon. The first definition of LDs relied on the computation of the arc length of particle trajectories as they evolve forward and backward in time.[59] Later, the method was extended to include other positive quantities. The methodology found several applications in different scientific areas, such as ocean currents, atmospheric sciences, and chemistry.[58,59]

LDs provide insight that appears to be linked with the the geometric pattern of structures that govern transport in phase space. Their definition and heuristic arguments explaining why they are effective are presented in Reference 58. A theoretical framework is discussed in Reference 60. However, the connection between LDs and geometric patterns governing the transport in phase space is controversial and largely disputed in the literature. Indeed, LDs are not derived from mathematically well defined variational principles, thus their relation to invariant manifolds is unclear and mathematically not well defined.[54,61] Moreover, LDs are not objective, i. e., structures resulting from the scalar field depend on the frame of the observer, whereas material curves such as periodic orbits are frame-indifferent.[62,63] Finally, counter-examples to the method of Lagrangian descriptors are discussed in the literature.[62]

Let's consider a general time-dependent vector field on $\mathbb{R}^n$

$$\frac{\mathrm{d}\mathbf{x}(t)}{\mathrm{d}t} = \mathbf{f}(\mathbf{x},t), \quad \text{with } \mathbf{x} \in \mathbb{R}^n, \quad \text{and } t \in \mathbb{R}. \tag{2}$$

Assuming the velocity field C^r ($r \geq 1$) in $\mathbf{x}$ and continuous in t, a unique solution allowing for linearization exists. Given the initial time t_0 and the integration time span $[t_0-\tau, t_0+\tau]$, the Euclidean arc length $\tilde{M}$ of the curve in the phase space defined by propagating $\mathbf{x}(t_0) = \mathbf{x}_0$ through Eq. (2) is[58]

$$\tilde{M}(\mathbf{x}_0, t_0, \tau) = \int_{t_0-\tau}^{t_0+\tau} \sqrt{\sum_{i=1}^{n} \left(\frac{\mathrm{d}x_i(t)}{\mathrm{d}t}\right)^2}\,\mathrm{d}t = \int_{t_0-\tau}^{t_0+\tau} \|\mathbf{f}(\mathbf{x},t)\|\mathrm{d}t. \tag{3}$$

Table 4. Class of LDs with integrand and norm.[58,60]

LD	$\lvert\mathcal{F}(\mathbf{x}(t))\rvert$	Integrand description	Norm
M_1	$\lVert\mathbf{v}(t)\rVert$	Magnitude of velocity	L^1
M_2	$\lVert\mathbf{a}(t)\rVert$	Magnitude of acceleration	L^1
$M_{3.1}$	$\lVert\mathbf{v}(t)\rVert$	Magnitude of velocity	$L^{1/2}$
$M_{3.2}$	$\lVert\mathbf{a}(t)\rVert$	Magnitude of acceleration	$L^{1/2}$
M_4	$\lVert\dot{\mathbf{a}}(t)\rVert$	Magnitude of acceleration derivative	L^1
M_5	$(\lvert\kappa\rvert+a)^{-1}$	Positive quantity related to curvature†	L^1
M_6	$\lVert\mathbf{x}(t)\rVert$	Magnitude of space state	L^1
M_7	$\lVert\mathbf{x}(t)\rVert$	Magnitude of space state	$L^{1/2}$
M_8	$\sum_{i=1}^{n}\lvert x_i(t)\rvert^p$	Sum of p-root terms‡	L^p

† With $\kappa=\dfrac{(\mathbf{v}\cdot\mathbf{v})(\mathbf{a}\cdot\mathbf{a})-(\mathbf{v}\cdot\mathbf{a})^2}{v^3}$ and $1\leq a\leq 5$ to avoid singularities.[58]

‡ It is suggested to choose $p=1/\tau$ (see Reference 60).

Results depend on the finite horizon chosen. $\tilde{M}$ can be computed appending its integrand to the space state equations with a zero initial value and propagating the extended dynamics. Trajectories propagated from close ICs remaining close as they evolve in time are expected to have similar $\tilde{M}$.[58] Differently, abrupt changes in the field are associated to separatrices of the dynamics. Such features are expected to exhibit a discontinuity in the derivative of $\tilde{M}$ along the direction perpendicular to the separatrix.[58,60]

There exist other positive intrinsic physical or geometrical properties of trajectories that can be integrated to successfully identify geometric patterns. The general formulation is[58]

$$\begin{cases} M(\mathbf{x}_0,t_0,\tau)=\displaystyle\int_{t_0-\tau}^{t_0+\tau}\lvert\mathcal{F}(\mathbf{x}(t))\rvert^{\gamma}\mathrm{d}t & \text{for}\quad \gamma\leq 1 \\ M(\mathbf{x}_0,t_0,\tau)=\Big(\displaystyle\int_{t_0-\tau}^{t^0+\tau}\lvert\mathcal{F}(\mathbf{x}(t))\rvert^{\gamma}\mathrm{d}t\Big)^{\frac{1}{\gamma}} & \text{for}\quad \gamma>1 \end{cases} \tag{4}$$

where γ defines the L^{γ} norm of the integrand. An extensive class of different LDs was defined in Reference 58 based on the integrand, the selected norm, and the integration interval (see Table 4). The definition of any function M_i can be broken in a natural way into forward and backward integration to obtain LDs M_i^f and M_i^b, respectively. The forward propagation should highlight stable manifolds of the dynamical system, while the backward one recovers unstable ones.[64] Their combination is capable to detect all invariant manifolds simultaneously. A key property common to all LDs is that they monotonically increase along a trajectory. Indeed, they are integrals of positive quantities. Being a heuristic approach, similarly to the finite-time Lyapunov exponent (FTLE), there is the possibility that they may fail in identifying LCSs correctly. This due to the lack of mathematical proofs providing necessary and/or sufficient conditions supporting LCSs existence.

STATEMENT OF THE PROBLEM

The backbone of a capture set is defined as the locus of points in a capture set $\mathcal{C}^1_{-1}$ also belonging to $\mathcal{C}^{n\gg 1}_{-1}$. This means that ICs constituting the backbone are expected to perform at least more than one (preferably many) revolution about the target planet. The advantage of the backbone is that it is

computed on the capture set $\mathcal{C}^1_{-1}$. This avoid propagating ICs for large final forward times typical of orbits belonging to capture sets featuring large revolution numbers n. Essentially, interesting capture solutions are inferred from the dynamical information obtained on a short finite horizon, so making the technique suitable for implementation on board spacecraft with limited resources akin to autonomous interplanetary CubeSats. The problem faced in this work can be stated as:

Problem. Find the locus of points in a capture set $\mathcal{C}^1_{-1}$ also belonging to capture sets $\mathcal{C}^{n\gg 1}_{-1}$. In particular, such locus of points is named backbone of the capture set and it is of interest because made of initial conditions performing many revolutions about the central body. A backbone is required to contain solutions belonging at least to capture sets $\mathcal{C}^{n\geq 5}_{-1}$.

Firstly, a methodology to derive a backbone must be developed. Secondly, according to the goal set in the problem statement, a backbone is required to contain solutions belonging to capture sets completing more than 5 revolutions.

METHODOLOGY

The approach to tackle the problem follows: 1) definition of LDs integrands suitable for astrodynamics purposes and computed over different forward and backward horizons; 2) computation of stationary points on several 1-dimensional sections of the forward LD scalar field propagated over a finite horizon comparable with weakly-stable set $\mathcal{W}_1$ and with constant initial pericenter radii r_{p0}; 3) construction of the backbone as the parametric curve of stationary points computed at step 2; 4) inference of capture set $\mathcal{C}^{n\gg 1}_{-1}$ from the backbone computed at step 3. In step 1, techniques capable of extracting dynamical insight about the system under study are exploited. This because the backbone must embed the qualitative long-term behavior of the sought $\mathcal{C}^{n\gg 1}_{-1}$ capture orbits.

Step 2 is heuristically justified in what follows. From the literature, abrupt changes in LD scalar fields are known to be separatrices for the dynamics.[58,60] Conversely, smooth islands in the scalar field appear to feature solutions with similar qualitative behavior. Our claim is that stationary points in 1-dimensional sections of a LD field correspond to solutions where the qualitative behavior is preserved if longer finite horizons are considered. Therefore, stationary points are thought to behave in the opposite way of abrupt changes. Consequently, they identify phase space locations where trajectories are more prone to retain their dynamical nature over time. To some extent, such trajectories are expected to be more robust as well.

Speaking of the problem at hand, not all stationary points of a 1-dimensional LD section are of interest. Indeed, only those confined within capture sets by the WSB are useful for the backbone computation. By assumption, the backbone is constructed interpolating a sequence of stationary points computed in the appropriate place of the phase space. Consequently, the backbone results being a curve expected to preserve its qualitative behavior on the long-term, so even over extended horizons. An educated initial guess granting the backbone confinement within a capture set is required for the success of the procedure. Once a sequence of stationary points computed on 1-dimensional LD sections is obtained, the backbone is derived in step 3 as a parametric curve interpolating the same stationary points. In step 4, ICs belonging to capture sets $\mathcal{C}^{n\gg 1}_{-1}$ are inferred sampling the backbone. Eventually, the performance of the method is assessed. LDs suitable for astrodynamics purposes and the backbone construction are explored in what follows.

Table 5. Finite horizons.

Subset	Finite horizon	
	Time	[days]
$\sim \mathcal{W}_1$	τ_1	304.11
$\sim \mathcal{W}_2$	τ_2	447.76
$\sim \mathcal{W}_3$	τ_3	597.21
$\sim \mathcal{W}_4$	τ_4	729.39
$\sim \mathcal{W}_5$	τ_5	893.21
$\sim \mathcal{W}_6$	τ_6	1023.82
$\sim \mathcal{X}_{-1}$	τ_{-1}	228.68

Lagrangian descriptors suitable for astrodynamics

Several LD integrands are proposed in References 58, 60 and reported in Table 4. However, alternative integrand definitions could be specified to address the specific needs of the problem at hand. Two integrands suitable for astrodynamics problems are introduced for this purpose. The first is a LD based on the Keplerian energy of the spacecraft with respect to the target body (i. e., Mars). This is named* M_9. The second descriptor, called M_{10}, considers a metric derived from the spacecraft angular momentum even in this case referred to the target body. In mathematical means, they are

$$M_9(\mathbf{x}_0, t_0, \tau_b, \tau_f) = \int_{t_0-\tau_b}^{t_0} \left| \frac{v^2}{2} - \frac{\mu_t}{r} \right|^{1/\tau_b} \mathrm{d}t + \int_{t_0}^{t_0+\tau_f} \left| \frac{v^2}{2} - \frac{\mu_t}{r} \right|^{1/\tau_f} \mathrm{d}t \tag{5}$$

$$M_{10}(\mathbf{x}_0, t_0, \tau_b, \tau_f) = \int_{t_0-\tau_b}^{t_0+\tau_f} \|\mathbf{r} \times \mathbf{v}\|^{1/2} \mathrm{d}t \tag{6}$$

where $\mathbf{x} = [\mathbf{r}^\top \mathbf{v}^\top]^\top$ is the state variable; r and v are the magnitudes of position vector $\mathbf{r}$ and velocity vector $\mathbf{v}$, respectively; μ_t is the gravitational parameter of the central body; τ_b and τ_f are the backward and forward finite horizons, respectively.

The choice of backward and forward finite horizons is key. In fact, extremely short finite horizons preclude revealing the underlying dynamical template of geometrical structures, so concealing transport patterns in the phase space.[60] Conversely, unreasonably lengthy horizons furnish excessive information to process, thereby jeopardizing the method and leading to undesired outcomes. The finite horizon choice being critical, a preliminary study is carried out to identify proper time spans for the LD scalar fields propagation. As a result, backward and forward horizons are selected as the escape time and aggregate revolution periods, respectively, of a reference capture orbit.

The reference orbit is that belonging to $\mathcal{C}_{-1}^6$ and exhibiting minimum regularity coefficient $\Delta S_{\%}$ out of 1×10^3 trajectories computed: at capture epoch t_0 set to December 9, 2023 at 12:00:00.00 (UTC), so maximizing $\mathcal{R}_c$;[16] with orbital plane defined by inclination and right ascension of the ascending node (RAAN) imposed to $i_0 = \Omega_0 = 0.2\pi$ rad, so maximizing Mars' capture ratio (see Figure 10 in Reference 16); setting osculating eccentricity $e_0 = 0.99$;[14] imposing true anomaly $\theta_0 = 0$ deg (i. e., assumed at pericenter); assuming constant initial pericenter radius $r_{p0} = 2.1$ LU; sampling 1×10^3 arguments of pericenter in the range $[230, 260]$ deg.

*Subscripts are assigned in continuity with those used in Table 4.

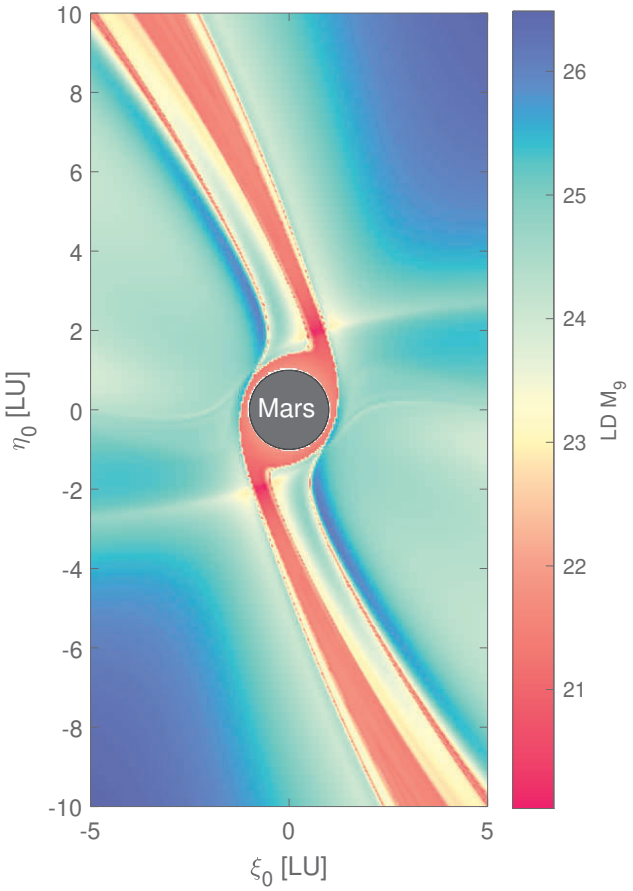

Figure 1. Energy based LD field $\mathcal{M}_9(\tau_{-1},\tau_6)$. Finite horizon comparable to capture set $\mathcal{C}^6_{-1}$. Initial time epoch t_0 set to December 9, 2023 at 12:00:00.00 (UTC). Nondimensional coordinates on the orbital plane $i_0 = \Omega_0 = 0.2\pi$ rad defined in the Mars-centered RTN@t_0 frame. Mars represented in black. Features of LD field resemble the typical shape of capture sets. Separatrices of the phase space recognized as abrupt changes.

The resulting reference capture orbit is not representative of the whole capture sets $\mathcal{C}^n_{-1}$ with $n = 1,\ldots,6$. In fact, BC orbits generally manifest different times of flight both for pre- and post-capture legs as detailed in Reference 57 and addressed in References 56, 65. Nevertheless, the reference capture orbit is representative at least of those trajectories exhibiting high post-capture regularity and performing a close approach to Mars at an approximate distance of 2.1 LU. These are the most interesting solutions from operational perspectives.

Forward and backward finite horizons associated to the reference capture orbit are collected in Table 5. Each finite horizon is representative of a subset whose propagation time span is comparable to that of the chosen finite horizon itself. An example LD scalar field is propagated over a finite horizon comparable to capture set $\mathcal{C}^6_{-1}$, so using $\tau_b = \tau_{-1}$ and $\tau_f = \tau_6$. For notation purposes, a LD scalar field is defined as $\mathcal{M}_i(\tau_b,\tau_f) := \{M_i(\mathbf{x}_0,t_0,\tau_b,\tau_f)|(\mathbf{x}_0,t_0) \in \Pi\}$, where Π is the set of ICs. LD field $\mathcal{M}_9(\tau_{-1},\tau_6)$ is shown in Figure 1 in Cartesian coordinates, while it is represented in Figure 2 using Keplerian elements. Patterns in Figure 1 resemble the usual shape of capture sets. Differently, dynamical features highlighted in Figure 2 mirror capture sets as plotted in Reference 57.

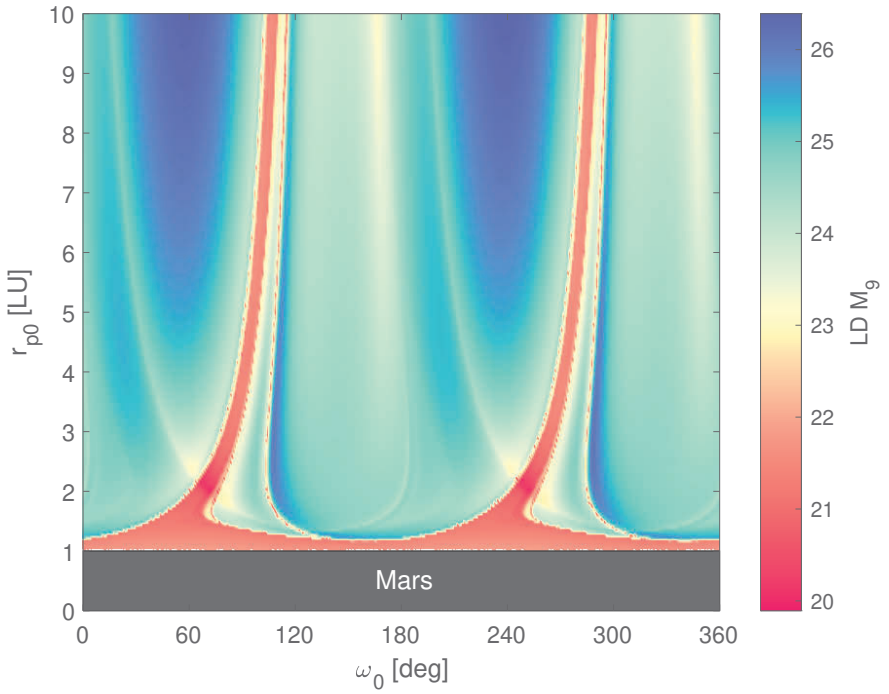

Figure 2. Energy based LD field $\mathcal{M}_9(\tau_{-1},\tau_6)$. Finite horizon comparable to capture set $\mathcal{C}^6_{-1}$. Initial time epoch t_0 set to December 9, 2023 at 12:00:00.00 (UTC). Radius of pericenter r_{p0} and argument of pericenter ω_0 at capture epoch t_0. Mars represented in black. Features of LD field resemble the shape of capture sets when represented as in Reference 57. Separatrices of the phase space recognized as abrupt changes.

Backbone construction

The selected LD is propagated over the finite horizon $(\tau_b,\tau_f)=(0,\tau_1)$, so for a time span comparable to revolution periods for weakly-stable set $\mathcal{W}_1$. Stationary points ω_0^* are searched between separatrices isolating weakly-stable orbits and on 1-dimensional sections along the initial argument of pericenter ω_0 at fixed initial pericenter radius r_{p0}. They are computed with the MATLAB®'s `fminunc` routine implementing a quasi-Newton optimization algorithm*. The optimization is performed with central finite differences, optimality tolerance set to 10^{-6}, and step tolerance equal to 10^{-10}. An initial guess ω_0^G is used to initialize the procedure. After getting the first stationary point ω_0^*, next points are computed solving optimization problems for increasing values of r_{p0} by steps of Δr_{p0}. New initial guesses are set equal to the last stationary point ω_0^* computed, so numerically continuing the sequence. Once the desired range of Mars distances is covered (i. e., enough stationary points are computed), the backbone is built as a parametric variational cubic spline curve†.[66]

*Visit `https://www.mathworks.com/help/optim/ug/fminunc.html` and `https://www.mathworks.com/help/optim/ug/choosing-the-algorithm.html` for additional details [last accessed Jan 5, 2023].

†For this purpose, MATLAB®'s `cscvn` routine is used, `https://www.mathworks.com/help/curvefit/cscvn.html` [last accessed Jan 5, 2023].

RESULTS

The backbone of the capture set $\mathcal{C}_{-1}^{1}$ is herewith constructed. Specifically, the backbone lying in the capture set portion developing into the interior subcorridor.[11] The backbone is computed after selecting what appears to be the most suited LD.

Lagrangian descriptor selection

The selection is carried out studying the trends of several 1-dimensional LD sections propagated over different finite horizons. The investigation is performed fixing the initial pericenter radius $r_{p0} = 2.1\,\mathrm{LU}$ and letting the initial argument of pericenter ω_0 vary in $[230, 260]\,\mathrm{deg}$. The selected finite horizons are $(\tau_b, \tau_f) = (0, \tau_1)$ and $(\tau_b, \tau_f) = (0, \tau_6)$, therefore those comparable to weakly-stable sets $\mathcal{W}_1$ and $\mathcal{W}_6$, respectively. Gradients along ω_0 computed with central finite differences are analyzed as well.[67] In Figure 3, trends for LDs specified in References 58, 60 are shown. Those for astrodynamics LDs are plotted in Figure 4. Both trends (i. e., blue curves on left y-axes) and gradients (i. e., red curves on right y-axes) are normalized to their maximum values for a fair comparison. As expected, dynamical features (e. g., abrupt changes, edges) are not completely developed yet in Figures 3(a) and 4(a). This because of the integration interval being insufficiently long.[60] LD trends are smooth and no remarkable discontinuities are detected in the gradients. Contrarily, many abrupt changes in the field and related discontinuities in the gradients are detected in Figures 3(b) and 4(b).

Among the investigated descriptors, the Keplerian energy based LD M_9 is preferred over other options for the following reasons. Firstly, M_9 seems extremely smooth when propagated on short horizons. This is a desirable property when solving optimization problems searching for stationary points. Unfortunately, some dynamical insight is lost due to the excessively short propagation interval, which is translated to accuracy loss in determining the exact backbone location. Hopefully, capture sets $\mathcal{C}_{-1}^{n \gg 1}$ can be still inferred from an approximation of the real backbone. Secondly, M_9 stationary points are expected to detect the phase space region featuring BC orbits with similar energetic behavior. Thirdly, a unique stationary point (i. e., a maximum) is visually detected* at $\omega_0 \approx 250\,\mathrm{deg}$, hence close to where the capture set branch developing the interior subcorridor is located.[11] Previous claims are confirmed by plots in Figure 5 where M_9 sections are inspected against subsets $\mathcal{W}$, $\mathcal{X}$, $\mathcal{K}$, $\mathcal{D}$, and $\mathcal{C}$. In fact, variations in the selected LD field does not match exactly the WSB (i. e., separatrices between sets). Nevertheless, the stationary point is correctly found within capture sets $\mathcal{C}_{-1}^{1}$ and $\mathcal{C}_{-1}^{6}$ (i. e., light green background). The stationary point (i. e., dashed vertical line) shifts to the left from Figure 5(a) to Figure 5(b), thereby proving the loss of dynamical insight for excessively short finite horizons. Nevertheless, the backbone can still be constructed even though some dynamical insight is lost.

Backbone

The backbone is built as a curve of stationary points computed on 1-dimensional sections of the Lagrangian descriptor M_9. They are computed on a finite horizon comparable to the revolution period of $\mathcal{C}_{-1}^{1}$ orbits. Before actually derive the backbone, some preliminary tests are performed to assure the effectiveness of the methodology. Specifically, 9 stationary points at various distances from Mars are computed with MATLAB®'s `fminunc` routine. In the peculiar problem under analysis, stationary points are maxima of 1-dimensional LD sections (see Figure 5). Consequently,

*Over finite horizon $(\tau_b, \tau_f) = (0, \tau_1)$, so $\sim \mathcal{W}_1$, this is true also for LDs $M_{3.2}$, M_7, and M_8.

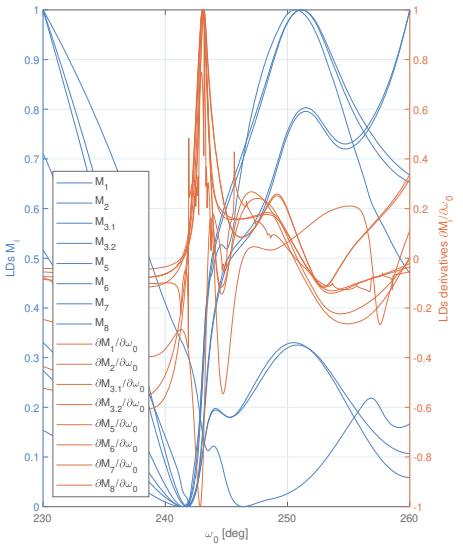

(a) Finite horizon $(\tau_b, \tau_f) = (0, \tau_1)$, so comparable to weakly stable set $\mathcal{W}_1$.

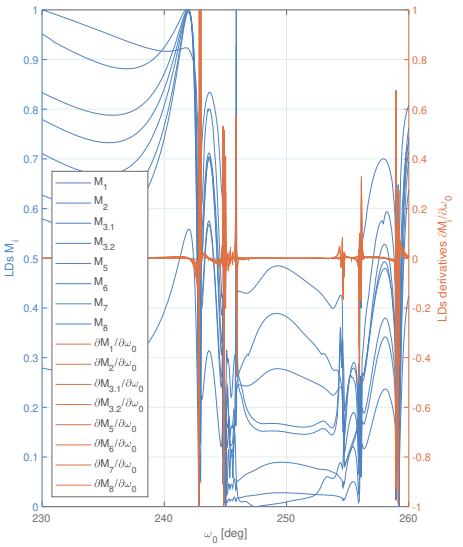

(b) Finite horizon $(\tau_b, \tau_f) = (0, \tau_6)$, so comparable to weakly stable set $\mathcal{W}_6$.

Figure 3. Study of 1-dimensional LD sections at constant initial pericenter radius $r_{p0} = 2.1\,\mathrm{LU}$. LDs defined by authors in Reference 58. LDs M_i (in blue, left y-axis) and gradients $\partial M_i/\partial\omega 0$ (in red, right y-axis) as a function of initial argument of pericenter ω_0, with $i = \{1, 2, 3.1, 3.2, 5, 6, 7, 8\}$. LDs M_i and gradients $\partial M_i/\partial\omega 0$ both normalized to their maximum values. Dynamical features are more developed for longer finite horizons.

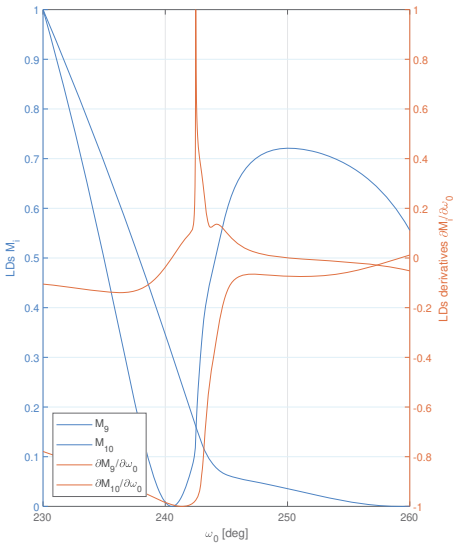

(a) Finite horizon $(\tau_b, \tau_f) = (0, \tau_1)$, so comparable to weakly stable set $\mathcal{W}_1$.

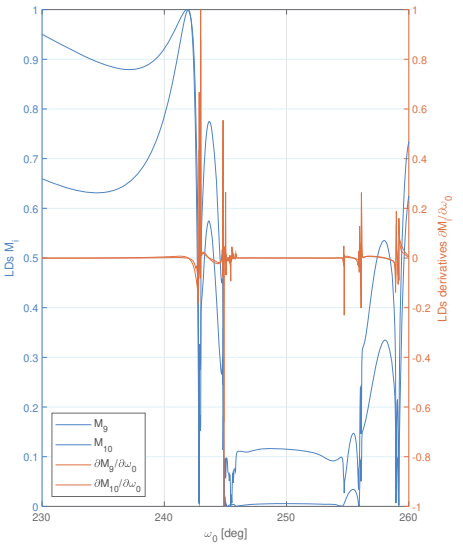

(b) Finite horizon $(\tau_b, \tau_f) = (0, \tau_6)$, so comparable to weakly stable set $\mathcal{W}_6$.

Figure 4. Study of 1-dimensional LD sections at constant initial pericenter radius $r_{p0} = 2.1\,\mathrm{LU}$. Astrodynamics based LDs. LDs M_i (in blue, left y-axis) and gradients $\partial M_i/\partial\omega 0$ (in red, right y-axis) as a function of initial argument of pericenter ω_0, with $i = \{9, 10\}$. LDs M_i and gradients $\partial M_i/\partial\omega 0$ both normalized to their maximum values. Dynamical features are more developed for longer finite horizons.

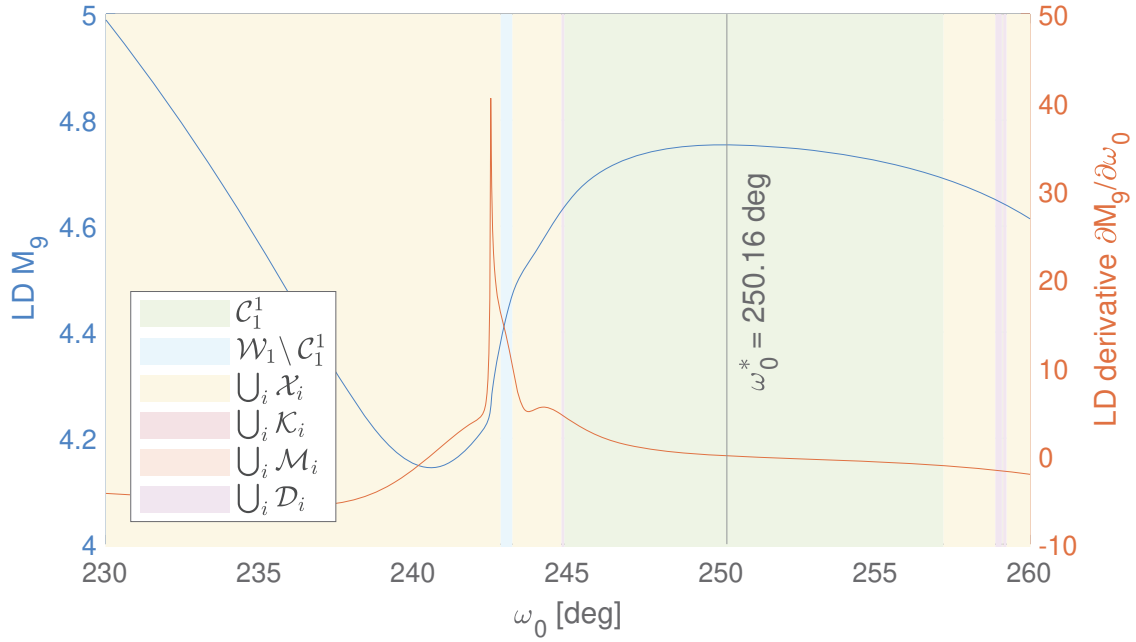

(a) Finite horizon $(\tau_b, \tau_f) = (0, \tau_1)$, so comparable to set $\mathcal{W}_1$.

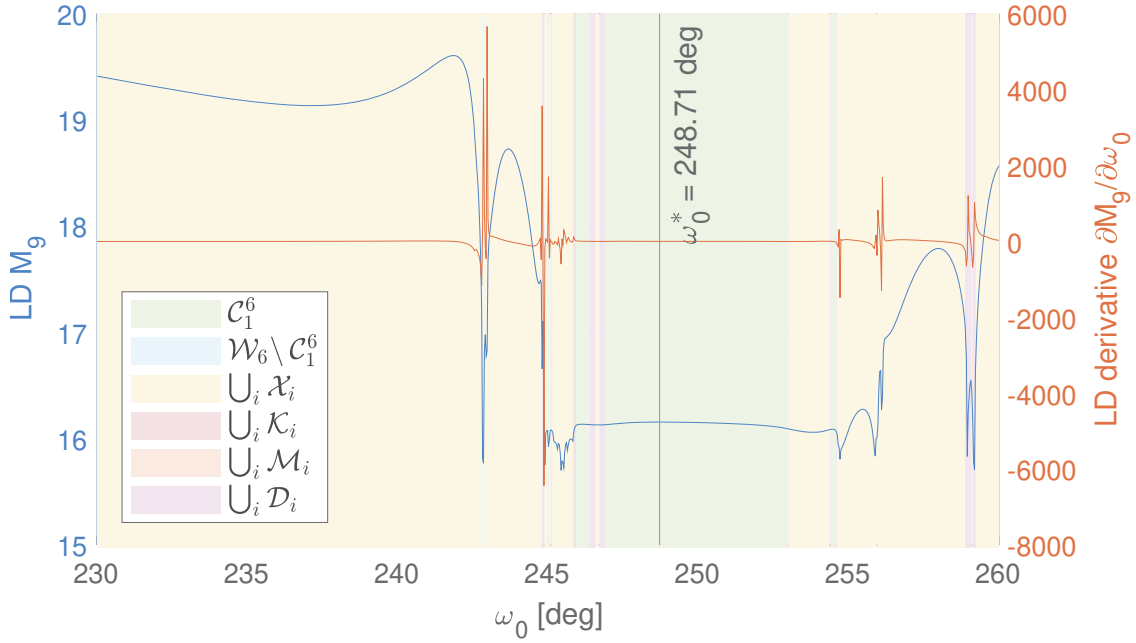

(b) Finite horizon $(\tau_b, \tau_f) = (0, \tau_6)$, so comparable to set $\mathcal{W}_6$.

Figure 5. Energy based LD M_9 (in blue, left y-axis) and gradient $\partial M_9/\partial\omega 0$ (in red, right y-axis) as a function of initial argument of pericenter ω_0 inspected against subsets $\mathcal{W}$, $\mathcal{X}$, $\mathcal{K}$, $\mathcal{D}$, and $\mathcal{C}$. Phase space 1-dimensional section at constant initial pericenter radius $r_{p0} = 2.1\,\mathrm{LU}$. LD stationary point of interest ω_0^* marked with dashed vertical line.

the cost function is defined as $f(\omega_0) = -M_i(r_{p0}, \omega_0, \tau_b, \tau_f)$ with r_{p0} fixed, $t_b = 0$ and $\tau_f = \tau_1$, so transforming stationary points into minima.

Results are shown in Figure 6, where the performance of LD M_9 is compared to that of M_8. LD M_8 is examined in contrast because of its proved capability of highlighting dynamical features thanks to the clever choice of setting the integrand exponent $p = 1/\tau$ (see Table 4).[60] In Figure 6, stationary points are marked as colored vertical dashed lines. Sections cover distances from 2 LU up to 6 LU. Both descriptors M_8 and M_9 decrease for larger distances from the target. At all distances, edges are not completely developed because of the short finite horizon chosen. However, limiting the finite horizon speeds up propagations of LDs and consequently the solution of the optimization problem. Descriptor M_9 behaves consistently across the various sections, remaining smooth and preserving its trend, see Figure 6(b). On the contrary, descriptor M_8 changes trend at large distances, so making difficult the computation of the stationary point. Remarkably, stationary points exceed the WSB for sections at $r_{p0} = 5.5$ LU and 6.0 LU.

Eventually, starting from the 1-dimensional section at $r_{p0} = 2.1$ LU, a sequence of $N_{\text{opt}} = 25$ optimization problems is solved for increasing r_{p0} values by steps of $\Delta r_{p0} = 1 \times 10^3$ km. Distances up to ≈ 9.2 LU are covered. The resulting backbone is presented in Figure 7. Scalar fields $\mathcal{M}_9(\tau_{-1}, \tau_1)$ and $\mathcal{M}_9(\tau_{-1}, \tau_6)$ are plotted in the background of Figures 7(a), 7(c) and Figures 7(b), 7(d), respectively. Results in Figures 7(a), 7(b) and Figures 7(c), 7(d) are represented on the $\omega_0 r_{p0}$-plane and $\xi_0\eta 0$-plane, respectively. The former are the initial Keplerian elements in the RTN@t_0 frame, while the latter are the Cartesian coordinates on the orbital plane defined by inclination and RAAN set to $i_0 = \Omega_0 = 0.2\pi$ rad.

In all four plots, the backbone remains confined by separatrices visible in the fields. This confirms how the dynamical information revealed by stationary points obtained over short finite horizons (i. e., $\sim \mathcal{W}_1$) embeds insight on the long-term qualitative behavior of capture orbits. ICs belonging to the backbone preserve their dynamical peculiarities even after more than 3 times the time span considered to construct the backbone (i. e., $\tau_6 \approx 3.4\tau_1$, see Table 5). Despite the additional effort in solving the sequence of optimization problems to get the stationary points, supplementary dynamical knowledge about the future evolution of the system is extracted from LD fields propagated on relatively short finite horizons. Therefore, clues on capture sets $\mathcal{C}_{-1}^{n \gg 1}$ are supposedly inferable from the backbone.

Performance analysis

A performance analysis is carried out to asses whether useful dynamical knowledge about $\mathcal{C}_{-1}^{n \gg 1}$ could be inferred or not from a backbone. Specifically, 10^3 ICs are uniformly sampled along the backbone constructed. Then, ICs are classified with GRATIS[24] into capture sets from $\mathcal{C}_{-1}^{1}$ up to $\mathcal{C}_{-1}^{10}$. The results in terms of absolute and relative number of BC orbits out of the whole sample are shown in Table 6. The totality of ICs belong to $\mathcal{C}_{-1}^{2}$, more than the 30% is classified into $\mathcal{C}_{-1}^{6}$, and almost the 20% is part of capture set $\mathcal{C}_{-1}^{10}$.

Capture set $\mathcal{C}_{-1}^{5}$ is studied in detail because of the goal set in the problem statement about inferring orbits classified into $\mathcal{C}_{-1}^{n \geq 5}$. Post-capture legs, and subcorridor $\check{\mathcal{S}}_{-1}^{5}$ up to $t_0 - 600$ days are propagated from the set of ICs sampled on the backbone and belonging to $\mathcal{C}_{-1}^{5}$. They are plotted in their entirety in Figure 8, while a magnification close to Mars' SOI is proposed in Figure 9. From the three views in Figure 8, the subcorridor $\check{\mathcal{S}}_{-1}^{5}$ (in light blue) appears much larger than that in Reference 11. Remarkably, the sample of ICs loses its capture properties starting from large distances with respect

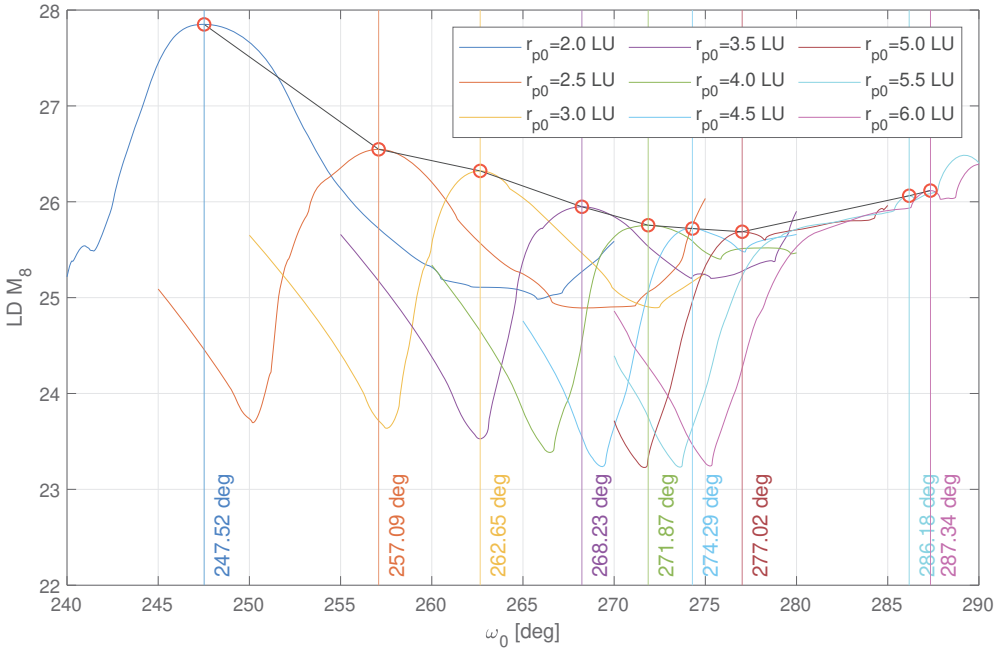

(a) Sections of LD M_8.

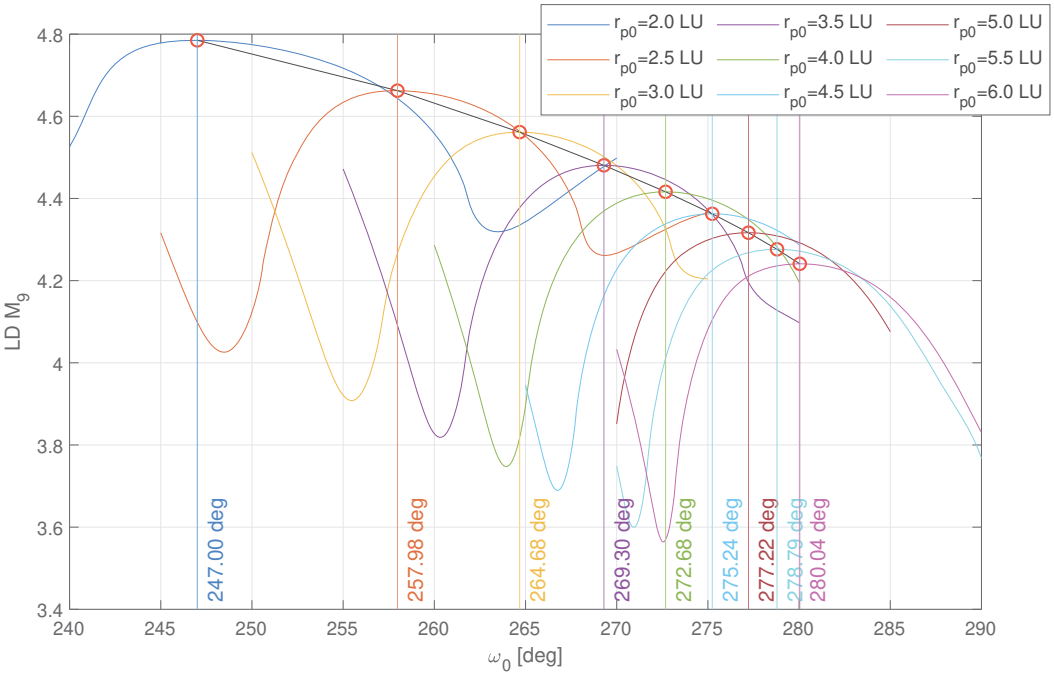

(b) Sections of Keplerian energy based LD M_9.

Figure 6. Stationary points ω_0^* of 1-dimensional LD sections evaluated at various initial pericenter radii r_{p0}. Stationary points marked as colored dashed vertical lines. Color code shown in the legend. Envelope of stationary points drawn as dashed black line. Finite horizon $(\tau_b, \tau_f) = (0, \tau_1)$, so comparable to weakly-stable set $\mathcal{W}_1$.

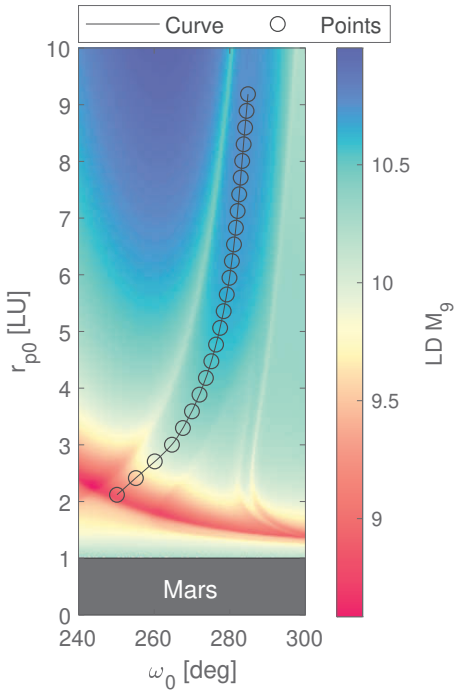

(a) Finite horizon $(\tau_b, \tau_f) = (\tau_{-1}, \tau_1)$, so $\sim \mathcal{C}^1_{-1}$; representation in $\omega_0 r_{p0}$-plane.

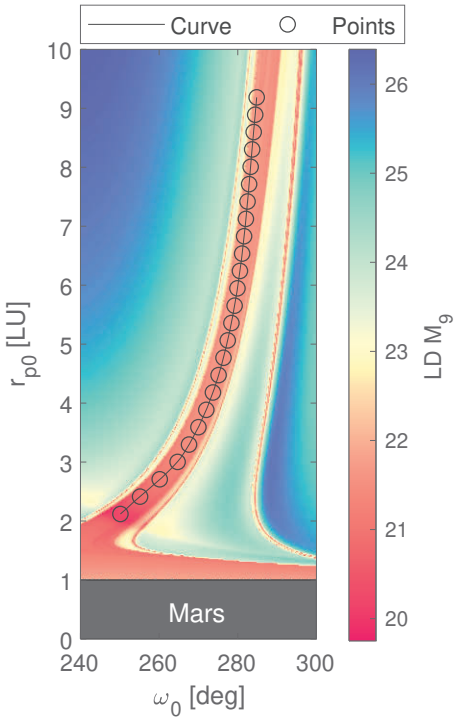

(b) Finite horizon $(\tau_b, \tau_f) = (\tau_{-1}, \tau_6)$, so $\sim \mathcal{C}^6_{-1}$; representation in $\omega_0 r_{p0}$-plane.

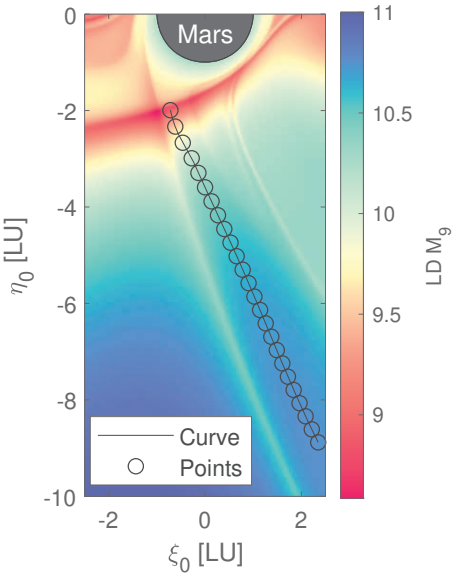

(c) Finite horizon $(\tau_b, \tau_f) = (\tau_{-1}, \tau_1)$, so $\sim \mathcal{C}^1_{-1}$; representation in $\xi_0 \eta_0$-plane.

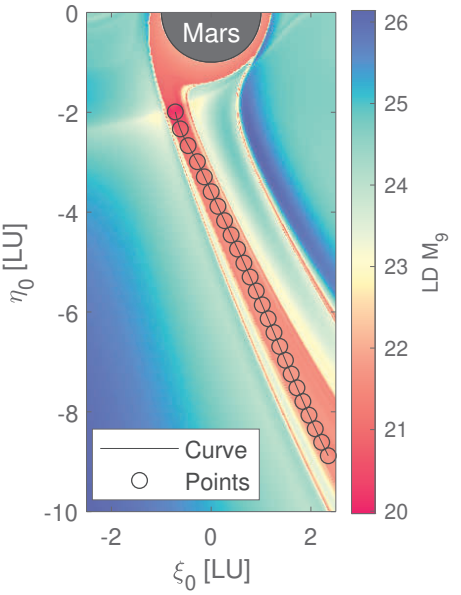

(d) Finite horizon $(\tau_b, \tau_f) = (\tau_{-1}, \tau_6)$, so $\sim \mathcal{C}^6_{-1}$; representation in $\xi_0 \eta_0$-plane.

Figure 7. Backbone (black solid line) inspected against energy based LD scalar fields $\mathcal{M}_9(\tau_{-1}, \tau_f)$ for two values of τ_f and two coordinate sets. Mars represented as black rectangle (on top) and black circle (on bottom). Stationary points marked as empty black circles. Backbone lies within regions confined by dynamic separatrices (abrupt changes) featured by LD fields propagated over both short ($\sim \mathcal{C}^1_{-1}$) and long ($\sim \mathcal{C}^6_{-1}$) finite horizons. Backbone starting from $r_{p0} = 2.1\,\mathrm{LU}$, with $N_{\mathrm{pnt}} = 25$ points by steps of $\Delta r_{p0} = 10^3\mathrm{km}$.

Table 6. Backbone performance. Analysis carried out sampling 10^3 backbone ICs.

Capture set $\mathcal{C}_{-1}^{n}$	Capture orbits	
Revolutions n	**Number**	**Percentage**
1	1000	100.0%
2	1000	100.0%
3	678	67.8%
4	446	44.6%
5	433	43.3%
6	337	33.7%
7	313	31.3%
8	304	30.4%
9	253	25.3%
10	199	19.9%

to the target. The most useful orbits from operational perspectives (i. e., those closely approaching Mars) retain the required dynamical behavior even on the long-term, thereby granting capture and successfully completing several revolutions about Mars.

CONCLUSION

The method presented in this paper is an alternative approach to present-day practices for designing BC orbits. The devised procedure leverages on the novel concept of capture set backbone from which ICs belonging to $\mathcal{C}_{-1}^{n\gg 1}$ are inferred. Construction of the backbone is made possible by exploiting the dynamical information embedded within LDs propagated on a short finite horizon. The knowledge extracted from metrics propagated over time intervals comparable to the revolution period typical of weakly-stable orbits in $\mathcal{W}_1$ is proved sufficient to deduce the location in the phase space of ICs performing several revolutions about Mars. The computationally demanding problem of designing orbits granting long-term temporary capture is unburden by maximizing the descriptor M_9 on selected 1-dimensional sections at constant initial pericenter radius, provided that the optimization is carried out within phase space regions bounded by the WSB. This novel design method being computationally light, it could potentially see implementation on board of autonomous, interplanetary CubeSats.

ACKNOWLEDGMENTS

This project has received funding from the European Research Council (ERC) under the European Union's Horizon 2020 research and innovation programme (Grant Agreement No. 864697).

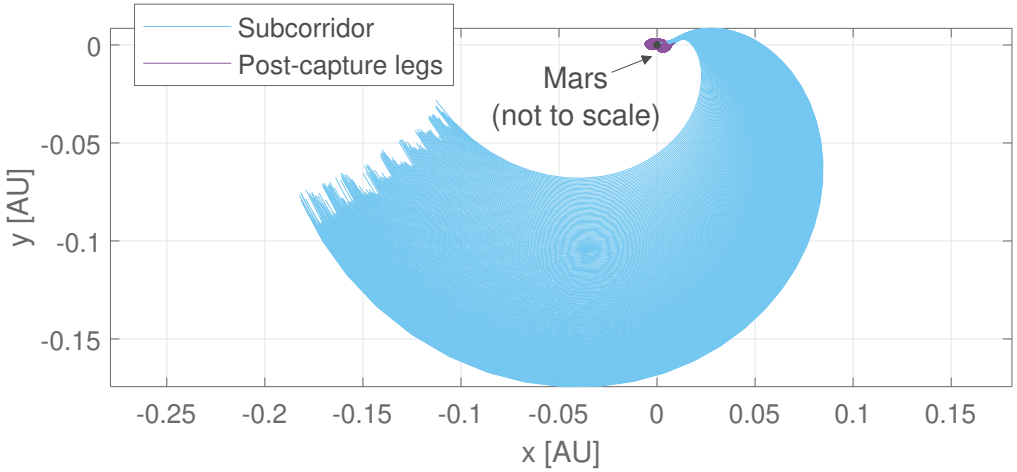

(a) View *xy*-plane.

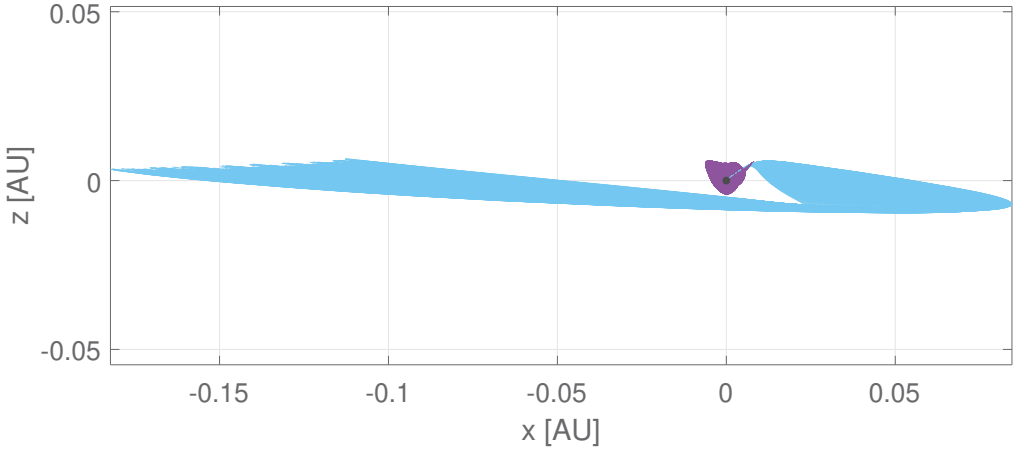

(b) View *xz*-plane.

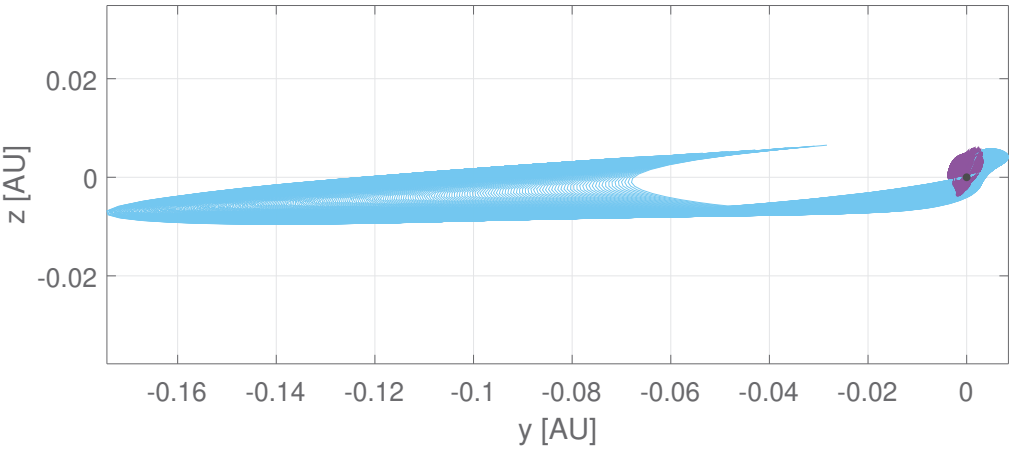

(c) View *yz*-plane.

Figure 8. Views in the physical space of subcorridor $\check{\mathcal{S}}^5_{-1}$ far from Mars built sampling the backbone. Subcorridor backward propagated from t_0 to t_0-600 days. Trajectories plotted in the Mars-centered ECLIPJ2000 frame.

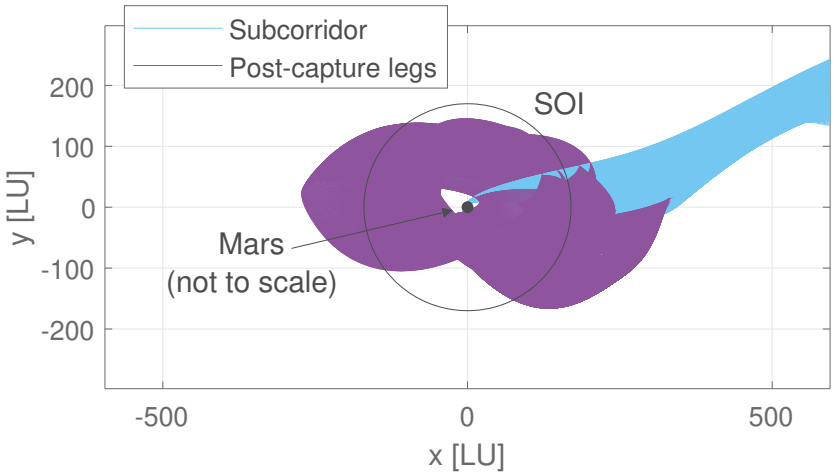

(a) View *xy*-plane.

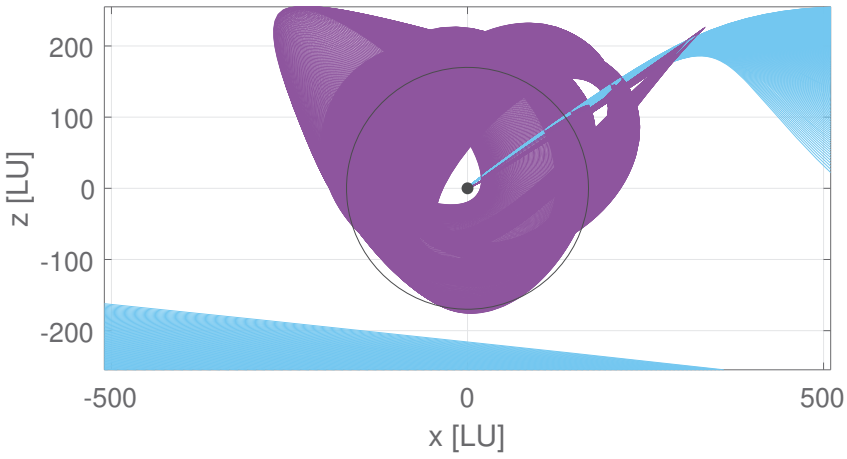

(b) View *xz*-plane.

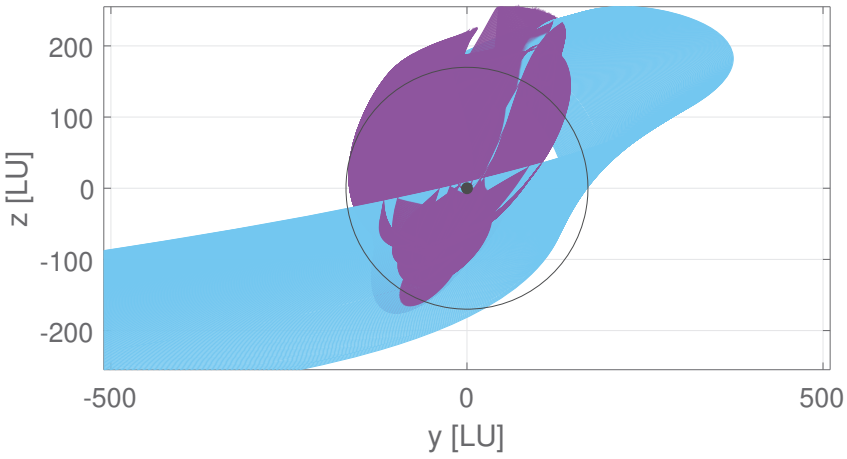

(c) View *yz*-plane.

Figure 9. Views in the physical space of subcorridor $\check{\mathcal{S}}^5_{-1}$ built sampling the backbone. Magnifications of subcorridor and post-capture legs close to Mars' SOI. Subcorridor backward propagated from t_0 to t_0-600 days. Trajectories plotted in the Mars-centered ECLIPJ2000 frame.

REFERENCES

[1] S. Bandyopadhyay, R. Foust, G. P. Subramanian, S.-J. Chung, and F. Y. Hadaegh, "Review of formation flying and constellation missions using nanosatellites," *Journal of Spacecraft and Rockets*, Vol. 53, No. 3, 2016, pp. 567–578, 10.2514/1.a33291.

[2] H. Kalita, E. Asphaug, S. Schwartz, and J. Thangavelautham, "Network of nano-landers for in-situ characterization of asteroid impact studies," 2017, 10.48550/arXiv.1709.02885.

[3] A. M. Hein, M. Saidani, and H. Tollu, "Exploring potential environmental benefits of asteroid mining," *69th International Astronautical Congress 2018*, 2018.

[4] G. Di Domenico, E. Andreis, A. C. Morelli, G. Merisio, *et al.*, "Toward self-driving interplanetary CubeSats: The ERC-funded project EXTREMA," *72nd International Astronautical Congress*, 2021.

[5] A. Morselli, G. Di Domenico, E. Andreis, A. C. Morelli, G. Merisio, *et al.*, "The EXTREMA orbital simulation hub: A facility for GNC testing of autonomous interplanetary CubeSat," *4S Symposium*, 2022, pp. 1–13.

[6] E. Andreis, V. Franzese, and F. Topputo, "An Overview of Autonomous Optical Navigation for Deep-Space CubeSats," *72nd International Astronautical Congress (IAC 2021)*, 2021, pp. 1–11.

[7] E. Andreis, V. Franzese, and F. Topputo, "Onboard orbit determination for deep-space CubeSats," *Journal of guidance, control, and dynamics*, 2022, pp. 1–14, 10.2514/1.G006294.

[8] E. Andreis, P. Panicucci, V. Franzese, and F. Topputo, "A Robust Image Processing Pipeline for Planets Line-Of-sign Extraction for Deep-Space Autonomous Cubesats Navigation," *44th AAS Guidance, Navigation and Control Conference*, 2022, pp. 1–19.

[9] A. C. Morelli, C. Hofmann, and F. Topputo, "A Homotopic Approach for Robust Low-Thrust Trajectory Design through Convex Optimization," *72nd International Astronautical Congress (IAC 2021)*, 2021, pp. 1–11.

[10] A. C. Morelli, C. Hofmann, and F. Topputo, "Robust Low-Thrust Trajectory Optimization Using Convex Programming and a Homotopic Approach," *IEEE Transactions on Aerospace and Electronic Systems*, 2021, 10.1109/TAES.2021.3128869.

[11] G. Merisio and F. Topputo, "Characterization of ballistic capture corridors aiming at autonomous ballistic capture at Mars," *2021 AAS/AIAA Astrodynamics Specialist Conference*, 2021, pp. 1–21.

[12] A. C. Morelli, G. Merisio, *et al.*, "A Convex Guidance Approach to Target Ballistic Capture Corridors at Mars," *44th AAS Guidance, Navigation and Control Conference*, 2022, pp. 1–24.

[13] G. Merisio and F. Topputo, "An algorithm to engineer autonomous ballistic capture at Mars," *73rd International Astronautical Congress (IAC 2022)*, 2022, pp. 1–16.

[14] F. Topputo and E. Belbruno, "Earth–Mars transfers with ballistic capture," *Celestial Mechanics and Dynamical Astronomy*, Vol. 121, No. 4, 2015, pp. 329–346, 10.1007/s10569-015-9605-8.

[15] Luo Z-F, F. Topputo, F. Bernelli Zazzera, and G. J. Tang, "Constructing ballistic capture orbits in the real Solar System model," *Celestial Mechanics and Dynamical Astronomy*, Vol. 120, No. 4, 2014, pp. 433–450, 10.1007/s10569-014-9580-5.

[16] Luo Z-F and F. Topputo, "Analysis of ballistic capture in Sun–planet models," *Advances in Space Research*, Vol. 56, No. 6, 2015, pp. 1030–1041, 10.1016/j.asr.2015.05.042.

[17] B. A. Archinal, M. F. A'Hearn, E. Bowell, A. Conrad, G. J. Consolmagno, R. Courtin, T. Fukushima, D. Hestroffer, J. L. Hilton, G. A. Krasinsky, *et al.*, "Report of the IAU working group on cartographic coordinates and rotational elements: 2009," *Celestial Mechanics and Dynamical Astronomy*, Vol. 109, No. 2, 2011, pp. 101–135, 10.1007/s10569-010-9320-4.

[18] C. Acton, "Ancillary data services of NASA's navigation and ancillary information facility," *Planetary and Space Science*, Vol. 44, No. 1, 1996, pp. 65–70, 10.1016/0032-0633(95)00107-7.

[19] C. Acton, N. Bachman, B. Semenov, and E. Wright, "A look towards the future in the handling of space science mission geometry," *Planetary and Space Science*, Vol. 150, 2018, pp. 9–12, 10.1016/j.pss.2017.02.013.

[20] R. S. Park, W. M. Folkner, J. G. Williams, and D. H. Boggs, "The JPL Planetary and Lunar Ephemerides DE440 and DE441," *The Astronomical Journal*, Vol. 161, No. 3, 2021, p. 105, 10.3847/1538-3881/abd414.

[21] F. Topputo, Y. Wang, C. Giordano, V. Franzese, H. Goldberg, F. Perez-Lissi, and R. Walker, "Envelop of reachable asteroids by M-ARGO CubeSat," *Advances in Space Research*, Vol. 67, No. 12, 2021, pp. 4193–4221, 10.1016/j.asr.2021.02.031.

[22] G. Aguiar and F. Topputo, "A Technique for Designing Earth–Mars Low-Thrust Transfers Culminating in Ballistic Capture," *7th International Conference on Astrodynamics Tools and Techniques (ICATT)*, 2018, pp. 1–8.

[23] C. Huang, J. C. Ries, B. D. Tapley, and M. M. Watkins, "Relativistic effects for near-Earth satellite orbit determination," *Celestial Mechanics and Dynamical Astronomy*, Vol. 48, No. 2, 1990, pp. 167–185, 10.1007/BF00049512.

[24] F. Topputo, D. A. Dei Tos, K. V. Mani, S. Ceccherini, C. Giordano, V. Franzese, and Y. Wang, "Trajectory design in high-fidelity models," *7th International Conference on Astrodynamics Tools and Techniques (ICATT)*, 2018, pp. 1–9.

[25] O. Montenbruck and E. Gill, *Satellite Orbits Models, Methods and Applications*. Springer, 2000, 10.1007/978-3-642-58351-3.

[26] P. J. Prince and J. R. Dormand, "High order embedded Runge–Kutta formulae," *Journal of computational and applied mathematics*, Vol. 7, No. 1, 1981, pp. 67–75, 10.1016/0771-050x(81)90010-3.

[27] E. Belbruno and J. Miller, "Sun-perturbed Earth-to-Moon transfers with ballistic capture," *Journal of Guidance, Control, and Dynamics*, Vol. 16, No. 4, 1993, pp. 770–775, 10.2514/3.21079.

[28] E. Belbruno and J. Carrico, "Calculation of weak stability boundary ballistic lunar transfer trajectories," *Astrodynamics Specialist Conference*, 2000, p. 4142, 10.2514/6.2000-4142.

[29] C. Circi and P. Teofilatto, "On the dynamics of weak stability boundary lunar transfers," *Celestial Mechanics and Dynamical Astronomy*, Vol. 79, No. 1, 2001, pp. 41–72, 10.1023/A:1011153610564.

[30] V. Ivashkin, "On trajectories of Earth–Moon flight of a particle with its temporary capture by the Moon," *Doklady Physics*, Vol. 47, Springer, 2002, pp. 825–827, 10.1134/1.1526433.

[31] E. Belbruno and J. Miller, "A ballistic lunar capture trajectory for the Japanese spacecraft Hiten," tech. rep., Jet Propulsion Laboratory, 1990. IOM 312/904-1731-EAB.

[32] G. Racca, A. Marini, L. Stagnaro, J. Van Dooren, L. Di Napoli, B. Foing, R. Lumb, J. Volp, J. Brinkmann, R. Grünagel, *et al.*, "SMART-1 mission description and development status," *Planetary and space science*, Vol. 50, No. 14-15, 2002, pp. 1323–1337, 10.1016/S0032-0633(02)00123-X.

[33] M. Chung, S. Hatch, J. Kangas, S. Long, R. Roncoli, and T. Sweetser, "Trans-lunar cruise trajectory design of GRAIL (Gravity Recovery and Interior Laboratory) mission," *AIAA/AAS Astrodynamics Specialist Conference*, 2010, p. 8384, 10.2514/6.2010-8384.

[34] J. Benkhoff, G. Murakami, W. Baumjohann, S. Besse, E. Bunce, M. Casale, G. Cremosese, K.-H. Glassmeier, H. Hayakawa, D. Heyner, *et al.*, "BepiColombo-Mission Overview and Science Goals," *Space Science Reviews*, Vol. 217, No. 8, 2021, pp. 1–56, 10.1007/s11214-021-00861-4.

[35] A. Schuster and R. Jehn, "Influence of the Mercury gravity field on the orbit insertion strategy of Bepi-Colombo," *Aerospace Science and Technology*, Vol. 39, 2014, pp. 546–551, 10.1016/j.ast.2014.06.003.

[36] Luo Z-F and F. Topputo, "Mars orbit insertion via ballistic capture and aerobraking," *Astrodynamics*, Vol. 5, No. 2, 2021, pp. 167–181, 10.1007/s42064-020-0095-4.

[37] C. Giordano and F. Topputo, "Aeroballistic Capture at Mars: Modeling, Optimization, and Assessment," *Journal of Spacecraft and Rockets*, 2022, pp. 1–15, 10.2514/1.A35176.

[38] Luo Z-F and F. Topputo, "Capability of satellite-aided ballistic capture," *Communications in Nonlinear Science and Numerical Simulation*, Vol. 48, 2017, pp. 211–223, 10.1016/j.cnsns.2016.12.021.

[39] D. A. Dei Tos, R. P. Russell, and F. Topputo, "Survey of Mars ballistic capture trajectories using periodic orbits as generating mechanisms," *Journal of Guidance, Control, and Dynamics*, Vol. 41, No. 6, 2018, pp. 1227–1242, 10.2514/1.g003158.

[40] E. Belbruno, "Lunar capture orbits, a method of constructing Earth Moon trajectories and the lunar GAS mission," *19th International Electric Propulsion Conference*, American Institute of Aeronautics and Astronautics, 1987, pp. 1–9, 10.2514/6.1987-1054.

[41] E. Belbruno, *Capture Dynamics and Chaotic Motions in Celestial Mechanics*. Princeton University Press, 2004, 10.1515/9780691186436.

[42] F. García and G. Gómez, "A note on weak stability boundaries," *Celestial Mechanics and Dynamical Astronomy*, Vol. 97, No. 2, 2007, pp. 87–100, 10.1007/s10569-006-9053-6.

[43] F. Topputo and E. Belbruno, "Computation of weak stability boundaries: Sun–Jupiter system," *Celestial Mechanics and Dynamical Astronomy*, Vol. 105, No. 1-3, 2009, pp. 3–17, 10.1007/s10569-009-9222-5.

[44] P. Sousa Silva and M. Terra, "Applicability and dynamical characterization of the associated sets of the algorithmic weak stability boundary in the lunar sphere of influence," *Celestial Mechanics and Dynamical Astronomy*, Vol. 113, No. 2, 2012, pp. 141–168, 10.1007/s10569-012-9409-z.

[45] F. Topputo, E. Belbruno, and M. Gidea, "Resonant motion, ballistic escape, and their applications in astrodynamics," *Advances in Space Research*, Vol. 42, No. 8, 2008, pp. 1318–1329, 10.1016/j.asr.2008.01.017.

[46] E. Belbruno, F. Topputo, and M. Gidea, "Resonance transitions associated to weak capture in the restricted three-body problem," *Advances in Space Research*, Vol. 42, No. 8, 2008, pp. 1330–1351, 10.1016/j.asr.2008.01.018.

[47] N. Hyeraci and F. Topputo, "Method to design ballistic capture in the elliptic restricted three-body problem," *Journal of guidance, control, and dynamics*, Vol. 33, No. 6, 2010, pp. 1814–1823, 10.2514/1.49263.

[48] E. Belbruno and J. Green, "When Leaving the Solar system: Dark matter makes a difference," *Monthly Notices of the Royal Astronomical Society*, Vol. 510, No. 4, 2022, pp. 5154–5163, 10.1093/mnras/stab3781.

[49] E. Belbruno, M. Gidea, and F. Topputo, "Weak stability boundary and invariant manifolds," *SIAM Journal on Applied Dynamical Systems*, Vol. 9, No. 3, 2010, pp. 1061–1089, 10.1137/090780638.

[50] E. Belbruno, M. Gidea, and F. Topputo, "Geometry of weak stability boundaries," *Qualitative Theory of Dynamical Systems*, Vol. 12, No. 1, 2013, pp. 53–66, 10.1007/s12346-012-0069-x.

[51] E. Belbruno, "Relation between solutions of the Schrödinger equation with transitioning resonance solutions of the gravitational three-body problem," *Journal of Physics Communications*, Vol. 4, No. 1, 2020, p. 015012, 10.1088/2399-6528/ab693f.

[52] F. Topputo, M. Vasile, and F. Bernelli-Zazzera, "Low energy interplanetary transfers exploiting invariant manifolds of the restricted three-body problem," *The Journal of the Astronautical Sciences*, Vol. 53, No. 4, 2005, pp. 353–372, 10.1007/BF03546358.

[53] G. Haller, "A variational theory of hyperbolic Lagrangian coherent structures," *Physica D: Nonlinear Phenomena*, Vol. 240, No. 7, 2011, pp. 574–598.

[54] G. Haller, "Lagrangian coherent structures," *Annual Review of Fluid Mechanics*, Vol. 47, 2015, pp. 137–162, 10.1146/annurev-fluid-010313-141322.

[55] A. Wittig, P. Di Lizia, R. Armellin, K. Makino, F. Bernelli-Zazzera, and M. Berz, "Propagation of large uncertainty sets in orbital dynamics by automatic domain splitting," *Celestial Mechanics and Dynamical Astronomy*, Vol. 122, No. 3, 2015, pp. 239–261, 10.1007/s10569-015-9618-3.

[56] M. Manzi and F. Topputo, "A Flow-informed Strategy for Ballistic Capture Orbit Generation," *Celestial Mechanics and Dynamical Astronomy*, Vol. 133, No. 11, 2021, pp. 1–16, 10.1007/s10569-021-10048-2.

[57] T. Caleb, G. Merisio, P. Di Lizia, and F. Topputo, "Stable sets mapping with Taylor differential algebra with application to ballistic capture orbits around Mars," *Celestial Mechanics and Dynamical Astronomy*, Vol. 134, No. 5, 2022, pp. 1–22, 10.1007/s10569-022-10090-8.

[58] A. M. Mancho, S. Wiggins, J. Curbelo, and C. Mendoza, "Lagrangian descriptors: A method for revealing phase space structures of general time dependent dynamical systems," *Communications in Nonlinear Science and Numerical Simulation*, Vol. 18, No. 12, 2013, pp. 3530–3557, 10.5194/npg-21-677-2014.

[59] C. Mendoza, A. Mancho, and S. Wiggins, "Lagrangian descriptors and the assessment of the predictive capacity of oceanic data sets," *Nonlinear Processes in Geophysics*, Vol. 21, 2014, pp. 677–689, 10.5194/npg-21-677-2014.

[60] C. Lopesino, F. Balibrea-Iniesta, V. J. García-Garrido, S. Wiggins, and A. M. Mancho, "A theoretical framework for Lagrangian descriptors," *International Journal of Bifurcation and Chaos*, Vol. 27, No. 01, 2017, pp. 1730001, 1–25, 10.1142/S0218127417300014.

[61] A. Hadjighasem, M. Farazmand, D. Blazevski, G. Froyland, and G. Haller, "A critical comparison of Lagrangian methods for coherent structure detection," *Chaos: An Interdisciplinary Journal of Nonlinear Science*, 2017, 10.1063/1.4982720.

[62] A. Ruiz-Herrera, "Some examples related to the method of Lagrangian descriptors," *Chaos: An Interdisciplinary Journal of Nonlinear Science*, 2015, 10.1063/1.4922182.

[63] A. Ruiz-Herrera, "Performance of Lagrangian descriptors and their variants in incompressible flows," *Chaos: An Interdisciplinary Journal of Nonlinear Science*, 2016, 10.1063/1.4966176.

[64] V. García Garrido, "A Tutorial on the Method of Lagrangian Descriptors," tech. rep., 2019, 10.6084/m9.figshare.11340818.v2.

[65] J. Tyler and A. Wittig, "Three-dimensional Lagrangian Coherent Structures in the Elliptic-Restricted Three-body Problem," *arXiv preprint arXiv:2209.11561*, 2022, 10.48550/arXiv.2209.11561.

[66] E. T. Y. Lee, "Choosing nodes in parametric curve interpolation," *Computer-Aided Design*, Vol. 21, No. 6, 1989, pp. 363–370, 10.1016/0010-4485(89)90003-1.

[67] A. Quarteroni, R. Sacco, and F. Saleri, *Numerical mathematics*. Springer New York, 2007, 10.1007/b98885.